ACS NANO

www.acsnano.org

ARTICLE

Self-Rectifying Resistive Memory with a Ferroelectric and 2D Perovskite Lateral Heterostructure

Jeonghyeon Son,[‡] Minsub Lee,[‡] Arindam Sannyal, Hojun Yun, Jaehui Cheon, Sumin Lee, Jong S. Park, Seok Ju Kang, Joonkyung Jang, and Beomjin Jeong*

Cite This: *ACS Nano* 2025, 19, 10796−10806

Read Online

ACCESS | Metrics & More | Article Recommendations | Supporting Information

ABSTRACT: **Integration of resistive switching and rectification functions in a single memory device is promising for high writing/readout accuracy with a simplified device architecture, but the realization remains challenging, especially with a low voltage operation. Herein, we developed self-rectifying resistive memory with a single memristive layer that can be operated at ultralow voltages with an excellent rectification ratio. The memristive layer consisted of a phase-separated lateral heterostructure of a ferroelectric polymer, poly(vinylidene fluoride-*co*-trifluoroethylene) [P(VDF-TrFE)], and a 2D halide perovskite, butylammonium lead iodide (BA_2PbI_4), which could be readily fabricated by spin-casting. Systematic characterization revealed that a lateral ferroelectric polarization from self-poled P(VDF-TrFE) could rectify the current flow into the BA_2PbI_4 channel. The resistive memory consisting of Ag/P(VDF-TrFE):BA_2PbI_4/indium tin oxide exhibited a high resistance switching ratio of $>10^6$ programmable at ±0.4 V and an excellent rectification ratio of $>10^6$ at ±0.1 V, along with a long data retention and stable endurance cycles.**

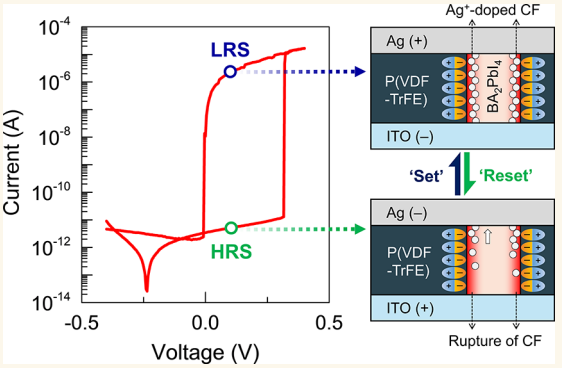

KEYWORDS: *ferroelectric, halide perovskites, self-rectifying memory, resistive memory, memristors*

INTRODUCTION

Two-terminal memristive switching devices, such as resistive random access memories (RRAM),[1−3] are gaining attention as emerging nonvolatile memory that can be implemented as a crossbar array structure. In a unit RRAM cell, data are stored as a high resistance state (HRS) or a low resistance state (LRS) in the memristive material. In the crossbar array, the memory cell is accessed to write or read the stored data. However, accurate writing and reading are hampered by a sneak current from neighboring cells. To suppress the sneak current, selectors have been integrated with the RRAM cells at the crosspoints.[4−7] For example, in the one diode and one resistor (1D-1R) structure, rectifying devices such as a PN junction or Schottky diode are stacked on the unit RRAM cell to use only one bias polarity and suppress current flow at the opposite bias polarity. However, the selector-integrated structures limit device architectures, increase circuit complexity, and require additional fabrication steps.[8]

Self-rectifying memristors (SRMs) have been thus actively pursued wherein a single device can simultaneously function as a memory and diode.[9] The SRMs resolve the sneak current issue without introducing additional device components, thus alleviating the aforementioned issues. Various memristive materials such as metal oxides,[10−28] silicon,[29−31] organic,[32] and ferroelectrics[33−38] have been applied as a switching layer in SRMs (Table S1, Supporting Information). Formation of a Schottky barrier at the interface between a memristive layer and an electrode is the representative method to render rectifying function to memristors (Table S1).[10−22,24−28,31,35,37,38] For SRMs with metal oxides, which are the most popular memristive materials, a simple method for self-rectification is to insert an additional oxide layer to build a high Schottky barrier between the oxide and the metal electrode, which can suppress a reverse current.[15−22,24−28] However, the switching voltages inevitably drop on the

Received: June 13, 2024
Revised: February 26, 2025
Accepted: February 26, 2025
Published: March 10, 2025

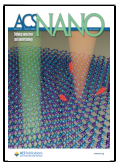

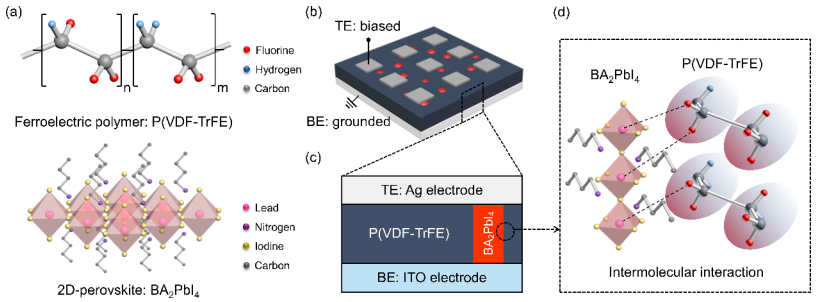

Figure 1. (a) Schematics of molecular structures of the ferroelectric P(VDF-TrFE) polymer and BA_2PbI_4 2D perovskite. (b) Schematic of a resistive memory device structure and (c) cross section of the device that represents a phase-separated lateral heterostructure with the BA_2PbI_4 crystal in the P(VDF-TrFE) matrix sandwiched between top Ag and bottom ITO electrodes. (d) Schematic of the P(VDF-TrFE) and BA_2PbI_4 interface, wherein the P(VDF-TrFE) chains are self-oriented by strong intermolecular interaction between P(VDF-TrFE) and BA_2PbI_4, leading to lateral ferroelectric polarization.

additional oxide layers, leading to a large voltage consumption. As a result, metal oxide SRMs that can be switched at sub-1 V have rarely been developed, and most of SRMs show the switching voltages around 3−12 V.[15−28] Single-layer metal oxide SRMs have also been reported, but most of the SRMs show switching voltages of 3−4 V, which are inherent to resistive switching mechanism of the metal oxides.[10−14] Other mechanisms for self-rectification have been suggested, such as the P−N junction in metal oxide or silicon oxide memristors, but exhibited switching voltages of a few volts.[23,30] Ferroelectric tunnel junctions or diodes have also been attempted for SRMs.[33−40] Resistive switching in ferroelectric SRMs occurs with the reversal of ferroelectric polarization, and self-rectification is induced by the formation of asymmetric potential barriers inside the ferroelectric switching layer or interfaces with electrodes (e.g., a metal-ferroelectric-semiconductor junction[33,35] or ionic defects generated during deposition[34,36]). Ferroelectric-semiconductor heterostructures, such as ferroelectric-semiconducting polymer blends[37−39] or lateral heterojunctions,[40] have also been reported to exhibit self-rectifying function. However, resistive switching of ferroelectric SRMs generally requires high switching voltages to overcome coercive fields for the electrical poling process. Further reduction in switching voltages may be pursued with development of novel resistive switching materials.[32]

In this regard, metal halide perovskites (MHPs) are promising as the resistive switching materials at low voltages thanks to their low energetic barrier for ion (or vacancy) migration.[41] Various kinds of MHPs have been applied to memristors with a simple metal/MHP/metal structure. For instance, Choi et al. demonstrated MHP memristors with Ag/$MAPbI_3$/Pt (MA = methylammonium) exhibiting ultralow set and reset voltages of +0.18 and −0.1 V, respectively.[42] Seo et al. developed two-dimensional (2D) MHP memristors with a device structure of Ag/BA_2PbI_4/Pt (BA = butylammonium) exhibiting set and reset voltages of +0.5 and −0.6 V, respectively.[43] However, these MHP memristors, including other cases reported in the literature,[41] are nonrectifying. Insertion of a rectifying oxide layer might be a viable route for developing MHP-based SRMs as demonstrated in metal oxide memristors. However, the voltage drop on the rectifying oxide is unavoidable. Moreover, fabrication of a multistack with MHPs is challenging because the oxides are generally processed at high-temperature processes, such as atomic layer deposition (e.g., Ta_2O_5 at 200 °C[15] or HfO_2 at 280 °C[16]), at which MHPs can be damaged or decomposed.[44] A single-layer SRM that can function as a memory and diode might offer a route for realization of a RRAM cell with low voltage operation in a simple device structure and a less complicated and nondestructive fabrication process. The single memristive layer for MHP-based SRMs may be achieved by a ferroelectric-semiconductor heterostructure, as previously demonstrated in phase-separated ferroelectric-semiconducting polymer blends (Table S1, refs 37−39). Several groups attempted mixing MHPs and ferroelectric polymers, such as poly(vinylidene fluoride-*co*-trifluoroethylene) [P(VDF-TrFE)], for assisting charge separation/transport and eventually enhancing device performance of solar cells and photodetectors.[45−48] These works suggest that compatibility of ferroelectric polymers with MHPs is excellent and beneficial for developing the ferroelectric-MHP heterostructure. Nevertheless, MHP-based SRMs with the ferroelectric-MHP heterostructure have yet to be attempted. Moreover, high voltage switching for polarization reversal in ferroelectric-semiconductor blends should be resolved.[39]

Herein, we developed a self-rectifying resistive memory with a single memristive layer, consisting of a phase-separated lateral heterostructure with ferroelectric P(VDF-TrFE) polymer and 2D MHP of BA_2PbI_4. The thin P(VDF-TrFE):BA_2PbI_4 blended film was readily fabricated by spin-casting. The memory device consisting of Ag/P(VDF-TrFE):BA_2PbI_4/ITO (ITO = indium tin oxide) exhibited excellent performance such as a high HRS/LRS ratio of $>10^6$ (at a read voltage of 0.1 V), a high rectification ratio of $>10^6$ (at ±0.1 V), programming and erasing voltages at ±0.4 V, a long data retention of $>10^4$ s, and switching endurance cycles of 200 times. It is revealed that the transition of the resistance states occurred from resistive switching inherent to BA_2PbI_4, while P(VDF-TrFE) endowed the rectifying function to the memory device. Systematic characterization of the P(VDF-TrFE):BA_2PbI_4 film revealed that the rectifying behavior originated from the self-polarization of P(VDF-TrFE) induced by intermolecular interaction with BA_2PbI_4 upon film processing. The self-established ferroelectric polarization suppressed the injection of charge carriers from Ag into BA_2PbI_4 at the negative voltage polarity, rendering BA_2PbI_4 resistive switching to occur in a self-rectifying manner with the high rectification ratio.

RESULTS AND DISCUSSION

A thin memristive film of P(VDF-TrFE) blended with BA_2PbI_4 was prepared by codissolution of the P(VDF-TrFE) polymer and BA_2PbI_4 precursors in a cosolvent at an optimized weight

https://doi.org/10.1021/acsnano.4c07869
ACS Nano 2025, 19, 10796−10806

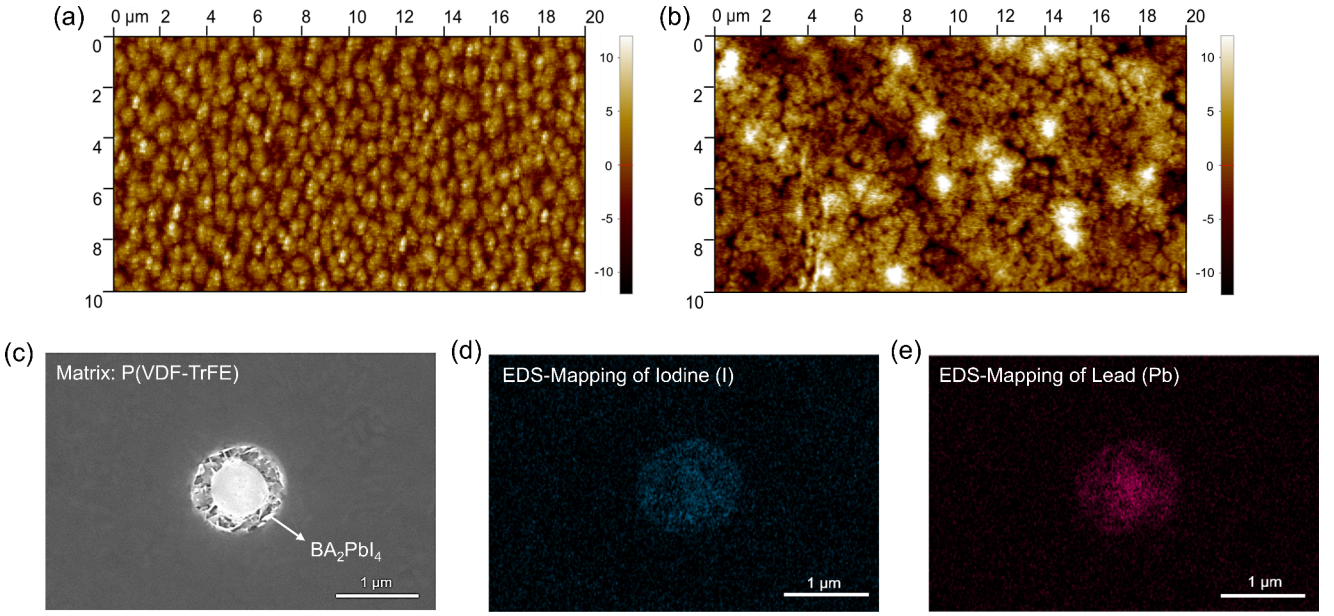

Figure 2. AFM height images of (a) pristine P(VDF-TrFE) and (b) P(VDF-TrFE):BA_2PbI_4 films (weight ratio = 1:0.37). (c) Magnified top-view SEM image to display BA_2PbI_4 crystals phase-separated in the P(VDF-TrFE) matrix and corresponding EDS mapping images of (d) I and (e) Pb elements.

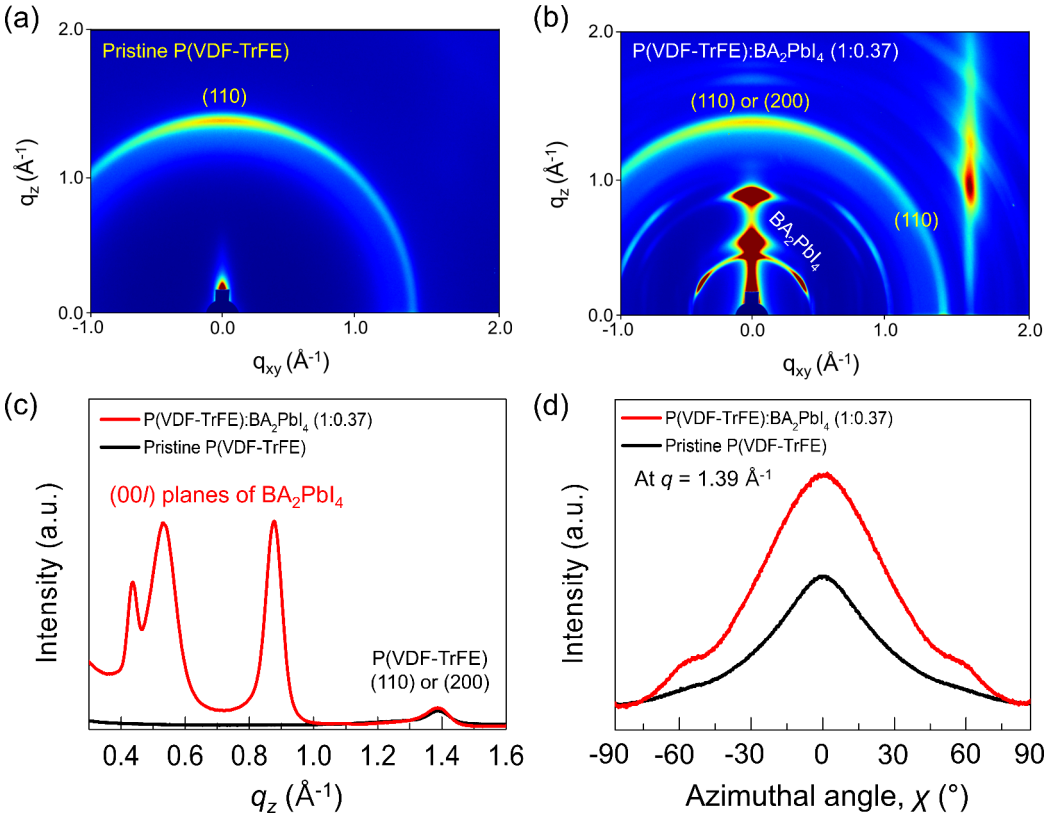

Figure 3. GIWAXS patterns of the (a) pristine P(VDF-TrFE) and (b) P(VDF-TrFE):BA_2PbI_4 (weight ratio = 1:0.37) films. (c) Line-cut profiles along the q_z direction and (d) azimuthal intensity profiles obtained from GIWAXS patterns in (a) and (b). In (c) and (d), black curves represent the data from the pristine P(VDF-TrFE) film, and red ones are for the P(VDF-TrFE):BA_2PbI_4 film (weight ratio = 1:0.37).

ratio of 1:0.37, followed by spin-coating on a bottom ITO/glass substrate and thermal annealing. The molecular structure of the P(VDF-TrFE) and BA_2PbI_4 is shown in Figure 1a. Ag was deposited as the top electrode on the P(VDF-TrFE):BA_2PbI_4 film. We used 2D BA_2PbI_4 perovskite as the resistive switching component thanks to its facile ion migration in a confined channel[43] and the P(VDF-TrFE) copolymer as a matrix because ferroelectric β-phase is readily formed upon spin-casting.[49−51] The P(VDF-TrFE):BA_2PbI_4 film is constituted of BA_2PbI_4 that is phase-separated in the P(VDF-

https://doi.org/10.1021/acsnano.4c07869
ACS Nano 2025, 19, 10796−10806

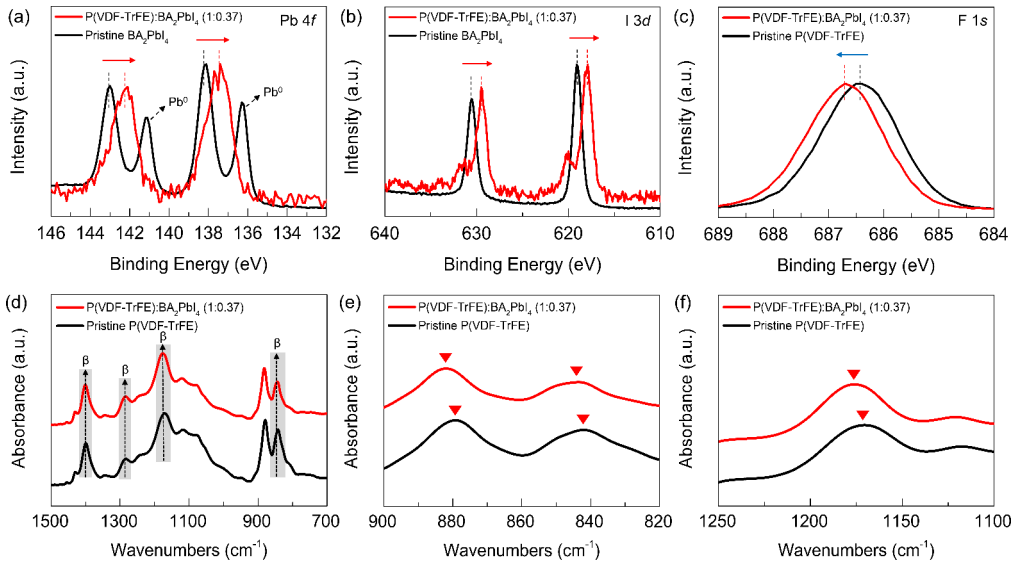

Figure 4. XPS spectra of (a) Pb 4f, (b) I 3d, and (c) F 1s binding energy from pristine P(VDF-TrFE) and P(VDF-TrFE):BA_2PbI_4 films (weight ratio = 1:0.37). Red arrows show the redshift, and blue ones show the blueshift in the binding energy of each core electron, when P(VDF-TrFE) was blended with BA_2PbI_4. (d) FT-IR spectra of pristine P(VDF-TrFE) and P(VDF-TrFE):BA_2PbI_4 (weight ratio = 1:0.37) films. IR peaks from β-phase signals of P(VDF-TrFE) are highlighted. (e, f) Magnified FT-IR spectra to examine the CF_2 vibration of P(VDF-TrFE). Red marks represent the characteristic IR absorption peaks from the CF_2 bonds.

TrFE) film, as schematically depicted in Figure 1b,c. As we will discuss later, the P(VDF-TrFE) polymer chains are self-aligned by strong intermolecular interactions with BA_2PbI_4 upon phase separation, as briefly illustrated in Figure 1d (the detailed crystal structure will be discussed later with structural characterization). The self-alignment gives rise to a polar *b*-axis of P(VDF-TrFE) oriented parallel to the substrate, resulting in spontaneous polarization of the P(VDF-TrFE) perpendicularly formed on the BA_2PbI_4 crystal surface. The self-established ferroelectric polarization allowed charge injection/transport through BA_2PbI_4 only at a positive voltage polarity while suppressing it at a negative polarity, leading to diode-like rectifying operation.

The phase-separated morphology of the P(VDF-TrFE):-BA_2PbI_4 film was examined by atomic force microscopy (AFM) and field emission scanning electron microscopy (FE-SEM), as shown in Figure 2. A pristine P(VDF-TrFE) film without BA_2PbI_4 displayed a typical β-phase morphology,[50] as shown in Figure 2a. In contrast, the P(VDF-TrFE):BA_2PbI_4 film exhibited a morphology with an island structure, as shown in Figure 2b. The island-like BA_2PbI_4 crystals with a diameter of ~1 μm were formed within the P(VDF-TrFE) film. When the content of the BA_2PbI_4 increased, the number of the BA_2PbI_4 crystals increased accordingly (Figure S1, Supporting Information), along with the expansion of the BA_2PbI_4 area (Figure S2, Supporting Information). The FE-SEM image of the P(VDF-TrFE):BA_2PbI_4 film revealed the polycrystalline morphology of the BA_2PbI_4, as shown in Figure 2c. The composition of BA_2PbI_4 was confirmed by energy-dispersive X-ray spectroscopy (EDS) mapping of I and Pb elements, as shown in Figures 2d and 2e, respectively. Strong elemental signals from the island-like crystals clarify successful formation of the BA_2PbI_4 crystals in the P(VDF-TrFE) film.

Microstructures of the P(VDF-TrFE):BA_2PbI_4 film were further characterized by using grazing-incidence wide-angle X-ray scattering (GIWAXS), as shown in Figure 3. The GIWAXS pattern of a pristine P(VDF-TrFE) film exhibited a strong arched reflection on the meridian (q = 1.39 Å^{-1}) with partial angular broadening, which corresponds to either (110) or (200) planes of ferroelectric β-phase crystals, as shown in Figure 3a.[52,53] Although the interplanar spacing of (110) and (200) is hard to decouple on the meridian due to the pseudohexagonal crystal structure of P(VDF-TrFE), we assign the reflection to the (110) plane in that the P(VDF-TrFE) film was deposited on a highly polar ITO/glass substrate.[52] This indicates that the chain axis of P(VDF-TrFE) (*c*-axis) is preferentially aligned parallel to the substrate. The P(VDF-TrFE):BA_2PbI_4 film exhibited mixed phases of the P(VDF-TrFE) and BA_2PbI_4 crystals with additional reflection peaks specified at q = 0.43 and 0.88 Å^{-1} corresponding to the (002) and (004) planes of BA_2PbI_4, respectively, as shown in Figure 3b,c.[54] The strong reflections of the (00*l*) planes along the meridian indicate that the BA_2PbI_4 sheets are stacked in an edge-on manner, as illustrated in Figure 1d. In contrast, the (00*l*) reflections along the meridian were less observed in a pure BA_2PbI_4 film (Figure S3, Supporting Information). Particularly noteworthy is that the reflection at q = 1.39 Å^{-1} on the meridian is slightly separated to azimuthal angles at $\chi = \pm 60°$, as shown in Figure 3d. This implies that the crystal orientation of P(VDF-TrFE) is altered when blended with BA_2PbI_4. Previous studies suggested that the azimuthal separation could be attributed to the preferential orientation of a polar *b*-axis of P(VDF-TrFE) parallel to the substrate.[52,53] The preferential orientation arises from the strong intermolecular interaction at the P(VDF-TrFE) and BA_2PbI_4 interfaces, as discussed next.

The intermolecular interaction between P(VDF-TrFE) and BA_2PbI_4 was investigated by X-ray photoelectron spectroscopy (XPS) and Fourier-transform infrared spectroscopy (FT-IR), as shown in Figure 4. The binding energy of Pb 4f electrons exhibited a redshift from 143.0 and 138.1 eV to 142.1 and 137.4 eV, respectively, as shown in Figure 4a. The binding energy of I 3d electrons of BA_2PbI_4 in the P(VDF-TrFE):BA_2PbI_4 film was also redshifted from 630.5 and

https://doi.org/10.1021/acsnano.4c07869
ACS Nano 2025, 19, 10796−10806

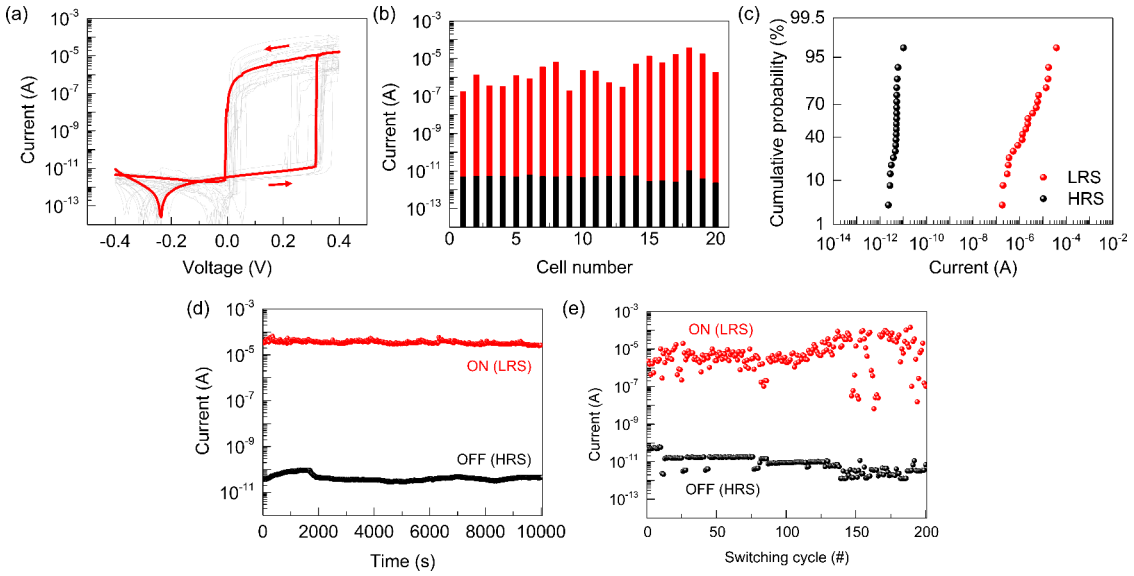

Figure 5. (a) Resistive switching *I*−*V* curves of the Ag/P(VDF-TrFE):BA_2PbI_4 (weight ratio = 1:0.37)/ITO device. Red arrows represent the scan direction. *I*−*V* curves from 20 devices are plotted together with the gray scale. (b) Statistics for a current ratio between LRS and HRS. (c) Cumulative probability of the current levels at the LRS and HRS. (d) Retention data and (e) switching cycle endurance of LRS and HRS. The HRS was programmed by sweeping from *V* = 0 to *V* = 0.4 V (represented by "ON"), whereas the LRS was achieved by sweeping to *V* = −0.4 V (represented by "OFF"). In all of the measurements, the read voltage was +0.1 V.

619.1 eV of the pristine BA_2PbI_4 film to 629.5 and 617.9 eV, respectively, as shown in Figure 4b. The XPS peak shift indicates the favorable intermolecular interaction between PbI_6 octahedral frameworks and H−C−F dipoles on polymer chains.[55] We note that metallic Pb^0 signals were only observed in the pristine BA_2PbI_4 film while they were absent in the P(VDF-TrFE):BA_2PbI_4 film, indicating that P(VDF-TrFE) retarded the decomposition of BA_2PbI_4. The blueshift in the binding energy of F 1s electrons of P(VDF-TrFE) in the P(VDF-TrFE):BA_2PbI_4 film, compared to a pristine P(VDF-TrFE) film, further supports the intermolecular interaction by H−C−F dipoles (Figure 4c). FT-IR spectra indicate that the ferroelectric β-phase was successfully formed in the P(VDF-TrFE):BA_2PbI_4 film, as strong IR absorption was observed at the peaks of 1400, 1290, 1187, and 840 cm^{-1}, as shown in Figure 4d.[56,57] The absorption profile of the β-phase peaks was almost the same as that of the pristine P(VDF-TrFE) film, implying that the crystallization of P(VDF-TrFE) was not hindered by the inclusion of BA_2PbI_4. In particular, the IR peaks at 1171, 879, and 841 cm^{-1} associated with stretching of the C−F bond exhibited blueshift, possibly due to the suppressed mechanical motion of the dipolar H−C−F bond by the electrostatic interaction with BA_2PbI_4.

Combined with the structural analysis with GIWAXS, the XPS and FT-IR results suggest that a polar *b*-axis of chain-folded P(VDF-TrFE) lamellar crystals is perpendicularly oriented from the surface of the BA_2PbI_4 channel into the P(VDF-TrFE) matrix, as schematically illustrated in Figure 1d (detailed structures are illustrated in Figure S11, Supporting Information). Previous reports indicate that MHPs possess lots of ionic defects on the crystallite surface such as abundant Pb^{2+} ionic defects, which can make Lewis acid−base interaction with negatively charged molecules.[58,59] In a similar way, electronegative F atoms can interact with Pb^{2+} on the surface of BA_2PbI_4 crystals, leading to preferential orientation of C−F bonds to BA_2PbI_4 through Pb^{2+}−F coordination, giving rise to the in-plane self-polarization. The preferential polar orientation leads to the formation of the lateral ferroelectric polarization that is self-established without external electrical poling (i.e., self-poling). We note that the self-poling effect induced by intermolecular interaction with low-dimensional nanomaterials is generally observed in various PVDF or P(VDF-TrFE) nanocomposites with $Ti_3C_2T_x$,[60,61] MoS_2 nanosheets,[62] carbon nanotubes,[63] and $BaTiO_3$ nanoparticles,[64] which further supports the proposed mechanism of self-polarization of P(VDF-TrFE) by BA_2PbI_4. The self-polarized P(VDF-TrFE) allows an electrical current only at a positive voltage polarity into BA_2PbI_4, while suppressing the current at a negative polarity, and thus endows rectifying function to the device, as discussed next.

The resistive switching behavior of the Ag/P(VDF-TrFE):BA_2PbI_4/ITO device was measured under a direct current (DC) voltage sweep in the range between +0.4 and −0.4 V, as shown in Figure 5a. The voltage was applied on the top Ag electrode, while the bottom ITO electrode was grounded, as shown in Figure 1b. Upon positive voltage sweeping from 0 to +0.4 V, abrupt resistance switching to LRS occurred at +0.32 V with an on current of ∼10^{-5} A (or 15.5 A/m^2, "set" process). Upon back-sweeping from +0.4 to −0.4 V, the device switched to HRS with an off current below ∼10^{-11} A (or 3.6 × 10^{-5} A/m^2, "reset" process), giving rise to an LRS/HRS (on/off) ratio of ∼10^6 (read at +0.1 V). Notably, the device exhibited rectifying behavior with a diode-like *I*−*V* curve with a high rectification ratio of 10^6 at ±0.1 V, wherein the current flowed only at the positive voltage range, while the current was significantly suppressed at the negative voltage range. The rectified state of the device in LRS was maintained unless the externally applied voltage decreased below −0.15 V; otherwise, the LRS transitioned to HRS, implying that the estimated "reset" voltage is around −0.15 V (Figure S4, Supporting Information). In striking contrast, the *I*−*V* curve of a pristine BA_2PbI_4 device represented bipolar conduction (Figure S5, Supporting Information). The rectification behavior was most clearly observed at an optimized ratio of

https://doi.org/10.1021/acsnano.4c07869
ACS Nano 2025, 19, 10796−10806

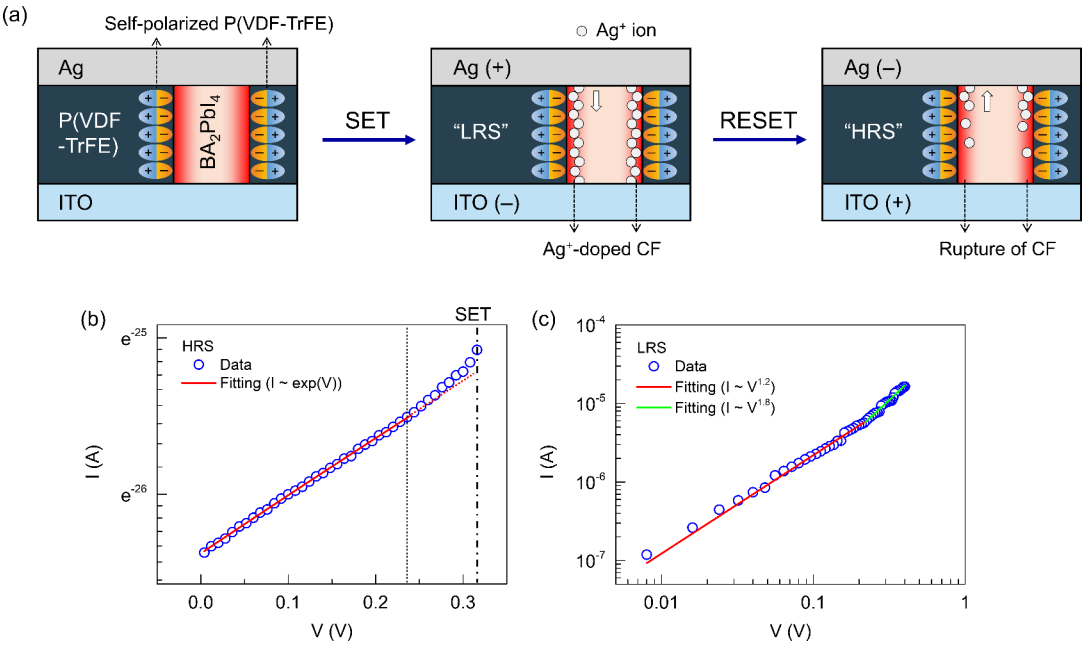

Figure 6. (a) Schematic illustration of the resistive switching process. Initially, P(VDF-TrFE) is self-polarized at the P(VDF-TrFE):BA_2PbI_4 interface. After set, Ag^+ ions migrate along the P(VDF-TrFE):BA_2PbI_4 interface and dope BA_2PbI_4, resulting in the formation of localized Ag^+-doped CFs. After reset, the Ag^+-doped CFs are ruptured. (b) Semilogarithmic plot of the $I-V$ data before SET ($0 < V < +0.32$ V). A solid red line is linear fitting with $I \sim \exp(V)$ from 0 to +0.24 V. A dotted red line is shown for visual guide. (c) Logarithmic plot of the $I-V$ data after SET ($+0.32$ V $< V < +0.4$ V). Solid red and green lines are linear fittings with $I \sim V^{1.2}$ and $I \sim V^{1.8}$, respectively.

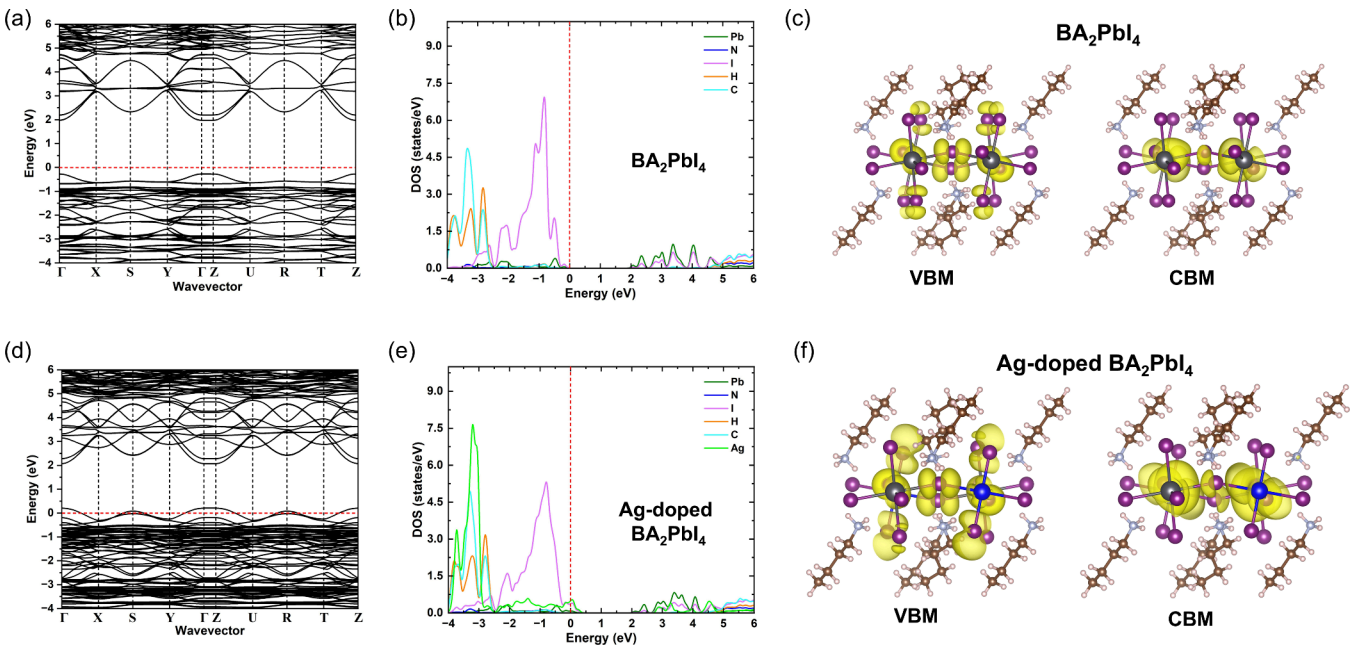

Figure 7. Band structures of (a) undoped BA_2PbI_4 and (d) Ag-doped BA_2PbI_4. The Fermi level is set to zero. Projected density of states of (b) undoped BA_2PbI_4 and (e) Ag-doped BA_2PbI_4. Partial charge densities at the VBM and CBM states of (c) undoped BA_2PbI_4 and (f) Ag-doped BA_2PbI_4. The isosurface values were taken to be 0.001 |e| $Å^{-3}$. Note that purple, gray, sky blue, brown, tan, and blue spheres represent I, Pb, N, C, H, and Ag, respectively.

P(VDF-TrFE):BA_2PbI_4 of 1:0.37 (Figure S5). The resistive switching behavior was optimized with the 105 nm-thick P(VDF-TrFE):BA_2PbI_4 layer (Figure S6, Supporting Information). The absence of ferroelectric switching peaks on the $I-V$ curves indicates that the resistive switching does not originate from the reversal of ferroelectric polarization but from the formation or rupture of conductive filaments (CFs), as discussed later. The $I-V$ measurement of 20 different cells revealed analogous RS behavior with excellent rectification, as shown in the $I-V$ curves in Figure 5a and LRS/HRS current ratios in Figure 5b. The average LRS/HRS current ratio from the 20 cells was 1.34×10^6, as shown in Figure 5c. The resistive switching behavior could be maintained for an extended period after 1-month storage at ambient conditions

https://doi.org/10.1021/acsnano.4c07869
ACS Nano 2025, 19, 10796−10806

with moderate variation in an LRS current and a set voltage, and stably operated at high temperatures up to 85 °C (Figure S7, Supporting Information). The device exhibited a long data retention of LRS and HRS for >10^4 s and endurance cycles of 200 times (read voltage = +0.1 V, programming = +0.4 V DC sweep, and erasing = −0.4 V DC sweep), as shown in Figure 5d,e. The device could also be operated by electrical pulses. However, the programming time is far longer than that of other memristive materials (Figure S8, Supporting Information). The relatively poor stability against electrical bias cycles is mainly attributed to the weak structural stability of MHPs against Joule heating[41,65] or a rough film surface that may lead to electrical short (Figure S1). Further studies are necessary for improving switching time and cyclic stability, such as structural engineering or modification of fabrication process.[66]

We propose the plausible mechanism of resistive switching behavior as electrochemical doping of BA_2PbI_4 by Ag^+ ions, as schematically depicted in Figure 6a. The abrupt change from HRS to LRS upon the set process indicates that the RS mechanism is likely to arise from the CF formation associated with Ag^+ ions, consistent with a previous study.[67] No resistive switching behavior was observed when the top electrode was replaced with an inert metal such as Au even at large voltages (Figure S9, Supporting Information). Doping-mediated resistive switching phenomena have recently been suggested as an alternative switching mechanism for MHP memristors.[41,68] Previous works demonstrated that Ag^+ ions can act as a p-type dopant for MHPs as shallow acceptors.[69−71] In our case, at the initial state, BA_2PbI_4 is a p-type semiconductor that exhibits high resistance. As shown in Figure 6b, a semi-logarithmic plot of the resistive switching $I-V$ curve in an HRS before SET (0 V ∼ +0.32 V) is fit linearly, which is indicative of hopping transport of charge carriers in BA_2PbI_4 and in accord with the previous result by Kim et al. (Supplementary Note 1).[72] Upon application of a positive voltage on top, Ag is expected to be electrochemically active and migrate as Ag^+ ions, by which BA_2PbI_4 is p-doped. The device switches from HRS to LRS because the hole injection barrier at Ag/Ag^+-doped BA_2PbI_4 is negligible as well as a large number of hole charges are accumulated (Figure S10, Supporting Information). The formation of Ag^+-doped CFs is likely to be localized near the P(VDF-TrFE):BA_2PbI_4 interface because of electrostatic attraction of Ag^+ ions by the lateral negative ferroelectric polarization,[73] as shown in Figure 6a. The LRS current follows ohmic conduction with space-charge-limited current (SCLC) behavior, as shown in Figure 6c. Detailed discussion on the device operation principle for set and reset processes is provided in Supplementary Note 1.

To clarify the proposed switching mechanism, we performed density functional theory (DFT) calculations to study the electronic properties of undoped and Ag-doped BA_2PbI_4. We found that both the valence band maximum (VBM) and conduction band minimum (CBM) of BA_2PbI_4 were located at the gamma (Γ) and Z points of the band structure, as shown in Figure 7a. This suggested that BA_2PbI_4 was a direct bandgap semiconductor with a calculated bandgap of 2.247 eV. We examined the density of states (DOS) of the BA_2PbI_4 to comprehend the electronic structures further. As shown in Figure 7b, the I ions comprised the majority of the VBM of BA_2PbI_4, while the Pb ions comprised the majority of the CBM. In addition, the VBM and CBM were slightly constituted of the Pb and I ions, respectively. Additionally, we computed the band decomposed partial charge density of the VBM and CBM. As seen in Figure 7c, the charges were primarily accumulated around the I and Pb ions in the VBM and CBM, respectively, corroborating the DOS analysis. The position of the CBM in the band structure did not significantly alter with Ag doping; however, as shown in Figure 7d, the VBM crossed the Fermi level, signifying the p-type doping of the Ag dopant. As shown in the DOS of Ag-doped BA_2PbI_4 in Figure 7e, the Ag dopant provided an additional band on top of the valence band, confirming the p-type doping. The I and Ag ions primarily constituted the VBM, with the Pb ions contributing only slightly. In the meantime, the Pb and Ag ions comprised the majority of the CBM, with the I ions contributing only slightly. As illustrated in Figure 7f, the I and Ag ions were the primary sites of charge accumulation in the VBM, while the Pb and Ag ions were the primary sites of charge accumulation in the CBM. These results support our claim that resistive switching is driven by the dynamic p-doping of BA_2PbI_4 by Ag^+ ions.

Rectification behavior is ascribed to a stray field developed by a lateral ferroelectric polarization (LFP), as illustrated in Figure S11 (Supporting Information).[74] According to Ghittorelli et al.'s work,[74] the stray field can be developed from an electrode to a ferroelectric-semiconductor interface (or vice versa) when a negative (or positive) LFP is established (Figure S11a). Similarly, the stray field is created from a Ag electrode to the P(VDF-TrFE):BA_2PbI_4 interface because a negative LFP is self-developed in our device (Figure S11b). When a positive voltage is applied on top, hole carriers are readily injected from Ag into the Ag^+-doped CFs. The stray field does not hamper the hole injection. When the voltage is reversed (negative on top), hole injection is expected to occur from the bottom ITO electrode. However, the hole injection is suppressed because the direction of the stray field is opposite at the bottom of the P(VDF-TrFE):BA_2PbI_4 interface (Figure S11b,c). Therefore, the hole charge carriers can transport in only one direction. It should be noted that typical ferroelectric diodes should be electrically poled at high voltages (normally, a few to tens of volts).[37−40,73] On the contrary, the electrical poling process is unnecessary in our device thanks to the self-poled P(VDF-TrFE), allowing the rectification at extremely low voltages. Detailed discussion on the rectification mechanism is provided in Supporting Information Note 1.

CONCLUSIONS

In summary, we developed self-rectifying resistive memory with a single memristive layer, consisting of the phase-separated lateral heterostructure with a ferroelectric polymer, P(VDF-TrFE), and 2D perovskite, BA_2PbI_4. The combination of facile ion migration characteristics of BA_2PbI_4 with self-poled P(VDF-TrFE) rendered the memristor operating at significantly low voltages with excellent memory and rectification performance, such as a high LRS/HRS ratio of >10^6 at a read voltage of +0.1 V, a high rectification ratio of >10^6 at ±0.1 V, PGM and ERS voltages at ±0.4 V, a long data retention of >10^4 s, and endurance switching cycles of >200 times. It should be noted that although thermal budget for the whole process for fabricating the Ag/P(VDF-TrFE):BA_2PbI_4/ITO device is small, which only requires thermal annealing of the as-deposited P(VDF-TrFE):BA_2PbI_4 film at 70 °C for 30 min, CMOS process compatibility remains a critical issue of this work, arising from the contamination issues from the organic components of the memristive layer during back-end-of-line (BEOL) steps. Nonetheless, our strategy provides a

https://doi.org/10.1021/acsnano.4c07869
ACS Nano 2025, 19, 10796−10806

simple but robust route to integrate memory and rectification function in a simplified structure with excellent device performance, potentially applicable for various combination of CMOS process-compatible materials such as ferroelectric HZO[75] and AlScN[36,76] and structurally robust memristive MHPs.[77]

EXPERIMENTAL SECTION

Materials. The P(VDF-TrFE) copolymer (VDF:TrFE = 70:30) was purchased from Solvay. BAI (99.9%), PbI_2 (99.9%), and DMF (anhydrous, 99.8%) were purchased from Sigma-Aldrich.

Device Fabrication. The P(VDF-TrFE):BA_2PbI_4 resistive memory with an architecture shown in Figure 1a was fabricated as follows: An ITO-coated glass substrate was sequentially cleaned in acetone and 2-propanol and treated with UV−O_3 (15 min for each process) before spin-coating the precursor solution. The precursor powders were dissolved in DMF at various weight ratios of P(VDF-TrFE) to BA_2PbI_4 (without BA_2PbI_4, 1:0.23, 1:0.3, 1:0.37, and 1:0.43) by vigorous stirring at 70 °C. In all the conditions, the ratio of BAI:PbI_2 was fixed to a 2:1 molar ratio. The precursor solution was spin-coated at 1500 rpm for 60 s. The as-spun film was dried at 70 °C for 60 min to remove the residual solvent. The thickness of the P(VDF-TrFE):BA_2PbI_4 films was around 350 nm. The fabrication was finished with the thermal evaporation of the top 100 nm-thick Ag top electrode using a shadow mask. The size of the device was estimated to be ∼380 μm^2.

Characterization and Electrical Measurements. The surface morphology was examined by noncontact-mode AFM (NX10, Park Systems, Korea) and FE-SEM (GEMINI500, Carl ZEISS, Germany). GIWAXS characterization was performed on a 6D UNIST-PAL line at the Pohang Accelerator Laboratory (Pohang, Korea). Monochromatized X-rays (λ = 1.0722 Å) were used to irradiate the films at grazing-incidence angles ranging from 0.14 to 0.16°. The GIWAXS samples were fabricated on Si substrates. The FT-IR spectra were acquired from an attenuated total reflectance mode IS50 instrument (Thermo Fisher Scientific, USA). The XPS spectra were obtained by an AXIS Supra instrument (Shimadzu, Japan). Electrical measurements of the resistive memory devices were carried out using a Keithley 4200-SCS analyzer at ambient conditions. The yield of functional devices was about 30% for $I-V$ measurements. Care should be taken for stable probe tip contact with the top Ag electrode.

Computational Methods. We performed density functional theory (DFT) calculations to study the electronic properties of undoped and Ag-doped BA_2PbI_4. We first constructed a 2 × 2 supercell of BA_2PbI_4 from the orthorhombic crystal structure of the *Pnma* space group. Next, we substituted one of the Pb ions with a Ag ion to model the Ag-doped BA_2PbI_4. The Vienna ab initio simulation package (VASP) was used for all the DFT calculations.[78,79] The projector-augmented wave (PAW) approach described the interactions between electrons and ions.[80] The generalized gradient approximation (GGA) with Perdew−Burke−Ernzerhof (PBE) represented the exchange−correlation energy.[81] The Pb $5d^{10}6s^26p^2$, Ag $4d^{10}5s^1$, I $5s^25p^5$, N $2s^22p^3$, and C $2s^22p^2$ electrons were defined as valence electrons. The cutoff energy for the plane wave basis set was chosen to be 520 eV. The Grimme (DFT+D3) approach was used to incorporate the dispersion correction.[82] The materials were optimized until the maximum force was <0.01 eV $Å^{-1}$. A gamma-centered 3 × 3 × 1 mesh was employed to sample the Brillouin zone.

ASSOCIATED CONTENT

Supporting Information

The Supporting Information is available free of charge at https://pubs.acs.org/doi/10.1021/acsnano.4c07869.

AFM and SEM images; GIWAXS pattern; reset voltage plots; resistive switching $I-V$ curves with various processing conditions; device stability test under ambient and thermal conditions; pulse $I-V$ measurement results; schematics for the energy band diagram of the device; schematics and notes for the resistive switching and self-rectification mechanism; table for the comparison of device performance from the literatures (DOCX)

AUTHOR INFORMATION

Corresponding Author

Beomjin Jeong − *School of Chemical Engineering and Department of Organic Material Science and Engineering, Pusan National University, Busan 46241, Republic of Korea;* orcid.org/0000-0002-6403-5275; Email: bjjeong@pusan.ac.kr

Authors

Jeonghyeon Son − *School of Chemical Engineering, Pusan National University, Busan 46241, Republic of Korea*

Minsub Lee − *School of Chemical Engineering, Pusan National University, Busan 46241, Republic of Korea*

Arindam Sannyal − *Department of Nanoenergy Engineering, Pusan National University, Busan 46241, Republic of Korea*

Hojun Yun − *Department of Energy and Chemical Engineering, Ulsan National Institute of Science and Technology (UNIST), Ulsan 44919, Republic of Korea*

Jaehui Cheon − *School of Chemical Engineering, Pusan National University, Busan 46241, Republic of Korea*

Sumin Lee − *School of Chemical Engineering, Pusan National University, Busan 46241, Republic of Korea*

Jong S. Park − *School of Chemical Engineering and Department of Organic Material Science and Engineering, Pusan National University, Busan 46241, Republic of Korea;* orcid.org/0000-0002-7624-9502

Seok Ju Kang − *Department of Energy and Chemical Engineering, Ulsan National Institute of Science and Technology (UNIST), Ulsan 44919, Republic of Korea;* orcid.org/0000-0002-9921-6674

Joonkyung Jang − *Department of Nanoenergy Engineering, Pusan National University, Busan 46241, Republic of Korea;* orcid.org/0000-0001-9028-0605

Complete contact information is available at: https://pubs.acs.org/10.1021/acsnano.4c07869

Author Contributions

‡J. S. and M. L. contributed equally to this work. J. S. and M. L. designed the experiments and conducted the characterizations and device measurements. A. S. and J. J. carried out theoretical calculations and analyzed the corresponding data. H. Y. and S. J. K. performed structural characterizations using GIWAXS. J. C. and S. L. helped in the preparation of materials for spectroscopic characterizations and analyzed the data. J. S. P. contributed to interpretation of the experimental results and provided the funding source. B. J. conceived the idea, supervised the project, and drafted the manuscript. All authors contributed to discussions of the results and assisted the manuscript preparation.

Notes

The authors declare no competing financial interest.

ACKNOWLEDGMENTS

This work was supported by the Basic Research Laboratory project granted from the National Research Foundation (NRF) funded by the Ministry of Science and ICT (no. RS-

2023-00221396). This work was also supported by a grant from the National Research Foundation (NRF) funded by the Ministry of Science and ICT (no. 2022R1F1A1076251).

REFERENCES

(1) Strukov, D. B.; Snider, G. S.; Stewart, D. R.; Williams, R. S. The missing memristor found. *Nature* **2008**, *453*, 80.
(2) Yang, J. J.; Strukov, D. B.; Stewart, D. R. Memristive devices for computing. *Nat. Nanotechnol.* **2013**, *8*, 13.
(3) Xia, Q.; Yang, J. J. Memristive crossbar arrays for brain-inspired computing. *Nat. Mater.* **2019**, *18*, 309.
(4) Cho, B.; Kim, T.-W.; Song, S.; Ji, Y.; Jo, M.; Hwang, H.; Jung, G.-Y.; Lee, T. Organic Memory: Rewritable Switching of One Diode−One Resistor Nonvolatile Organic Memory Devices. *Adv. Mater.* **2010**, *22*, 1228.
(5) Wang, G.; Lauchner, A. C.; Lin, J.; Natelson, D.; Palem, K. V.; Tour, J. M. High-Performance and Low-Power Rewritable SiO_x 1 kbit One Diode−One Resistor Crossbar Memory Array. *Adv. Mater.* **2013**, *25*, 4789.
(6) Li, C.; Hu, M.; Li, Y.; Jiang, H.; Ge, N.; Montgomery, E.; Zhang, J.; Song, W.; Dávila, N.; Graves, C. E.; Li, Z.; Strachan, J. P.; Lin, P.; Wang, Z.; Barnell, M.; Wu, Q.; Williams, R. S.; Yang, J. J.; Xia, Q. Analogue signal and image processing with large memristor crossbars. *Nat. Electron.* **2018**, *1*, 52.
(7) Upadhyay, N. K.; Sun, W.; Lin, P.; Joshi, S.; Midya, R.; Zhang, X.; Wang, Z.; Jiang, H.; Yoon, J. H.; Rao, M.; Chi, M.; Xia, Q.; Yang, J. J. A Memristor with Low Switching Current and Voltage for 1S1R Integration and Array Operation. *Adv. Electron. Mater.* **2020**, *6*, No. 1901411.
(8) Seok, J. Y.; Song, S. J.; Yoon, J. H.; Yoon, K. J.; Park, T. H.; Kwon, D. E.; Lim, H.; Kim, G. H.; Jeong, D. S.; Hwang, C. S. A Review of Three-Dimensional Resistive Switching Cross-Bar Array Memories from the Integration and Materials Property Points of View. *Adv. Funct. Mater.* **2014**, *24*, 5316.
(9) Ren, S.; Dong, A.; Yang, L.; Xue, Y.; Li, J.; Yu, Y.; Zhou, H.; Zuo, W.; Li, Y.; Cheng, W.; Miao, X. Self-Rectifying Memristors for Three-Dimensional In-Memory Computing. *Adv. Mater.* **2024**, *36*, No. 2307218.
(10) Gao, S.; Zeng, F.; Li, F.; Wang, M.; Mao, H.; Wang, G.; Song, C.; Pan, F. Forming-free and Self-Rectifying Resistive Switching of the Simple Pt/TaOx/n-Si Structure for Access Device-Free High-Density Memory Application. *Nanoscale* **2015**, *7*, 6031−6038.
(11) Hsu, C. C.; Wang, S. Y.; Lin, Y. S.; Chen, Y. T. Self-Rectifying and Interface-Controlled Resistive Switching Characteristics of Molybdenum Oxide. *J. Alloys Compd.* **2019**, *779*, 609−617.
(12) Wu, Z.; Zhang, X.; Shi, T.; Wang, Y.; Wang, R.; Lu, J.; Wei, J.; Zhang, P.; Liu, Q.Convertible Volatile and non-Volatile Resistive Switching in a Self-Rectifying Pt/TiOx/Ti Memristor. *2021 5th IEEE Electron Devices Technology & Manufacturing Conference (EDTM)*; IEEE: Chengdu, China, April 8−11, 2021; pp 1− 3.
(13) Lim, B. M.; Lee, Y. M.; Yoo, C. S.; Kim, M. S.; Kim, J.; Kim, S.; Yang, J. J.; Lee, H.-S. High-Reliability and Self-Rectifying Alkali Ion Memristor through Bottom Electrode Design and Dopant Incorporation. *ACS Nano* **2024**, *18*, 6373−6386.
(14) Park, M. H.; Jeong, J. H.; Kim, W.; Park, S.; Lim, B. M.; Lee, H.-S.; Kang, S. J. A facile solution processible self-rectifying and sub-1 V operating memristor via oxygen vacancy gradient within a TiO_2 single layer. *J. Mater. Chem. C* **2024**, *12*, 6881−6892.
(15) Yoon, J. H.; Song, S. J.; Yoo, I.-H.; Seok, J. Y.; Yoon, K. J.; Kwon, D. E.; Park, T. H.; Hwang, C. S. Highly Uniform, Electroforming-Free, and Self-Rectifying Resistive Memory in the Pt/Ta_2O_5/HfO_{2-x}/TiN Structure. *Adv. Funct. Mater.* **2014**, *24*, 5086.
(16) Li, J.; Ren, S. g.; Li, Y.; Yang, L.; Yu, Y.; Ni, R.; Zhou, H.; Bao, H.; He, Y.; Chen, J.; Jia, H.; Miao, X. Sparse matrix multiplication in a record-low power self-rectifying memristor array for scientific computing. *Sci. Adv.* **2023**, *9*, No. eadf7474.
(17) Luo, Q.; Zhang, X.; Hu, Y.; Gong, T.; Xu, X.; Yuan, P.; Ma, H.; Dong, D.; Lv, H.; Long, S.; Liu, Q.; Liu, M. Self-Rectifying and Forming-Free Resistive-Switching Device for Embedded Memory Application. *IEEE Electron Device Lett.* **2018**, *39*, 664−667.
(18) Pi, S.; Li, C.; Jiang, H.; Xia, W.; Xin, H.; Yang, J. J.; Xia, Q. Memristor crossbar arrays with 6-nm half-pitch and 2-nm critical dimension. *Nat. Nanotechnol.* **2019**, *14*, 35.
(19) Jang, Y. H.; Han, J.; Kim, J.; Kim, W.; Woo, K. S.; Kim, J.; Hwang, C. S. Graph Analysis with Multifunctional Self-Rectifying Memristive Crossbar Array. *Adv. Mater.* **2023**, *35*, No. 2209503.
(20) Ren, S. G.; Ni, R.; Huang, X. D.; Li, Y.; Xue, K. H.; Miao, X. S. Pt/Al_2O_3/TaO_X/Ta Self-Rectifying Memristor With Record-Low Operation Current (<2 pA), Low Power (fJ), and High Scalability. *IEEE Trans. Electron Devices* **2022**, *69*, 838.
(21) Lee, J. H.; Park, J. H.; Dongale, T. D.; Kim, T. G. Vacancy-modulated self-rectifying characteristics of NiO_x/Al_2O_3-based nanoscale ReRAM devices. *J. Alloys Compd.* **2020**, *821*, No. 153247.
(22) Wu, M.-C.; Chen, J.-Y.; Ting, Y.-H.; Huang, C.-Y.; Wu, W.-W. A Novel High-Performance and Energy-Efficient RRAM Device with Multi-Functional Conducting Nanofilaments. *Nano Energy* **2021**, *82*, No. 105717.
(23) Wu, C.; Li, X.; Xu, X.; Lee, B. W.; Chae, S. C.; Liu, C. Self-rectifying resistance switching memory based on a dynamic p−n junction. *Nanotechnology* **2021**, *32*, No. 085203.
(24) Zhao, Y.; Lou, Z.; Hu, J.; Li, Z.; Xu, L.; Chen, Z.; Xu, Z.; Wang, T.; Wu, M.; Ying, H.; An, M.; Li, W.; Lin, X.; Zheng, X. Scalable Layer-Controlled Oxidation of Bi_2O_2Se for Self-Rectifying Memristor Arrays With sub-pA Sneak Currents. *Adv. Mater.* **2024**, *36*, No. 2406608.
(25) Yoon, J. H.; Kim, K. M.; Song, S. J.; Seok, J. Y.; Yoon, K. J.; Kwon, D. E.; Park, T. H.; Kwon, Y. J.; Shao, X.; Hwang, C. S. Pt/Ta_2O_5/HfO_{2-x}/Ti Resistive Switching Memory Competing with Multilevel NAND Flash. *Adv. Mater.* **2015**, *27*, 3811−3816.
(26) Kim, K. M.; Zhang, J.; Graves, C.; Yang, J. J.; Choi, B. J.; Hwang, C. S.; Li, Z.; Williams, R. S. Low-Power, Self-Rectifying, and Forming-Free Memristor with an Asymmetric Programing Voltage for a High-Density Crossbar Application. *Nano Lett.* **2016**, *16*, 6724.
(27) Jeon, K.; Kim, J.; Ryu, J. J.; Yoo, S. J.; Song, C.; Yang, M. K.; Jeong, D. S.; Kim, G. H. Self-rectifying resistive memory in passive crossbar arrays. *Nat. Commun.* **2021**, *12*, 2968.
(28) Cheong, W. H.; Jeon, J. B.; In, J. H.; Kim, G.; Song, H.; An, J.; Park, J.; Kim, Y. S.; Hwang, C. S.; Kim, K. M. Demonstration of Neuromodulation-inspired Stashing System for Energy-efficient Learning of Spiking Neural Network using a Self-Rectifying Memristor Array. *Adv. Funct. Mater.* **2022**, *32*, No. 2200337.
(29) Kim, K. H.; Hyun Jo, S.; Gaba, S.; Lu, W. Nanoscale Resistive Memory with Intrinsic Diode Characteristics and Long Endurance. *Appl. Phys. Lett.* **2010**, *96*, No. 053106.
(30) Li, C.; Han, L.; Jiang, H.; Jang, M. H.; Lin, P.; Wu, Q.; Barnell, M.; Yang, J. J.; Xin, H. L.; Xia, Q. Three-dimensional crossbar arrays of self-rectifying Si/SiO_2/Si memristors. *Nat. Commun.* **2017**, *8*, 15666.
(31) Kim, S.; Cho, S.; Park, B. G. Fully Si Compatible SiN Resistive Switching Memory with Large Self-Rectification Ratio. *AIP Adv.* **2016**, *6*, No. 015021.
(32) Yao, Z.; Pan, L.; Liu, L.; Zhang, J.; Lin, Q.; Ye, Y.; Zhang, Z.; Xiang, S.; Chen, B. Simultaneous implementation of resistive switching and rectifying effects in a metal-organic framework with switched hydrogen bond pathway. *Sci. Adv.* **2019**, *5*, No. eaaw4515.
(33) Lee, H.-S.; Park, H.-H. Tunneling Electroresistance Effect with Diode Characteristic for Cross-Point Memory. *ACS Appl. Mater. Interfaces* **2016**, *8*, 15476−15481.
(34) Goh, Y.; Hwang, J.; Kim, M.; Jung, M.; Lim, S.; Jung, S.-O.; Jeon, S.High Performance and Self-Rectifying Hafnia-Based Ferroelectric Tunnel Junction for Neuromorphic Computing and TCAM Applications. *2021 IEEE International Electron Devices Meeting (IEDM)*; IEEE, 2021; pp 17.2.1−17.2.4.
(35) Ma, M.; Lin, G.; Shen, R.; Xu, J.; Qian, H.; Gu, J.; Liu, H.; Zhang, H.; Yu, X.; Liu, Y.; Chen, J.; Jin, C.; Han, G. Resistance Switching and Carrier Transport Mechanisms of HfO_2-Based

https://doi.org/10.1021/acsnano.4c07869
ACS Nano 2025, 19, 10796−10806

Ferroelectric Diode. *IEEE Trans. Electron Devices* **2024**, *71*, 3959−3963.
(36) Kim, K. H.; Han, Z.; Zhang, Y.; Musavigharavi, P.; Zheng, J.; Pradhan, D. K.; Stach, E. A.; Olsson, R. H.; Jariwala, D. Multistate, Ultrathin, Back-End-of-Line-Compatible AlScN Ferroelectric Diodes. *ACS Nano* **2024**, *18*, 15925−15934.
(37) Asadi, K.; de Leeuw, D. M.; de Boer, B.; Blom, P. W. M. Organic non-volatile memories from ferroelectric phase-separated blends. *Nat. Mater.* **2008**, *7*, 547.
(38) Seufert, L.; HassanpourAmiri, M.; Gkoupidenis, P.; Asadi, K. Crossbar array of artificial synapses based on ferroelectric diodes. *Adv. Electron. Mater.* **2021**, *7*, No. 2100558.
(39) Asadi, K. Resistance Switching in Two-Terminal Ferroelectric-Semiconductor Lateral Heterostructures. *Appl. Phys. Rev.* **2020**, *7*, No. 021307.
(40) Feng, G.; Zhu, Q.; Liu, X.; Chen, L.; Zhao, X.; Liu, J.; Xiong, S.; Shan, K.; Yang, Z.; Bao, Q.; Yue, F.; Peng, H.; Huang, R.; Tang, X.; Jiang, J.; Tang, W.; Guo, X.; Wang, J.; Jiang, A.; Dkhil, B.; Tian, B.; Chu, J.; Duan, C. A Ferroelectric Fin Diode for Robust Non-Volatile Memory. *Nat. Commun.* **2024**, *15*, 513.
(41) Lee, S.; Son, J.; Jeong, B. Ion Dynamics in Metal Halide Perovskites for Resistive-Switching Memory and Neuromorphic Memristors. *Mater. Today Electron.* **2024**, *9*, No. 100114.
(42) Choi, J.; Park, S.; Lee, J.; Hong, K.; Kim, D. H.; Moon, C. W.; Park, G. D.; Suh, J.; Hwang, J.; Kim, S. Y.; Jung, H. S.; Park, N. G.; Han, S.; Nam, K. T.; Jang, H. W. Organolead Halide Perovskites for Low Operating Voltage Multilevel Resistive Switching. *Adv. Mater.* **2016**, *28*, 6562−6567.
(43) Seo, J.-Y.; Choi, J.; Kim, H.-S.; Kim, J.; Yang, J.-M.; Cuhadar, C.; Han, J. S.; Kim, S.-J.; Lee, D.; Jang, H. W.; Park, N.-G. Wafer-scale reliable switching memory based on 2-dimensional layered organic−inorganic halide perovskite. *Nanoscale* **2017**, *9*, 15278.
(44) Jeong, B.; Han, H.; Park, C. Micro- and Nanopatterning of Halide Perovskites Where Crystal Engineering for Emerging Photoelectronics Meets Integrated Device Array Technology. *Adv. Mater.* **2020**, *32*, No. 2000597.
(45) Zhang, C.; Wang, Z.; Yuan, S.; Wang, R.; Li, M.; Jimoh, M. F.; Liao, L.; Yang, Y. Polarized Ferroelectric Polymers for High-Performance Perovskite Solar Cells. *Adv. Mater.* **2019**, *31*, No. 1902222.
(46) Jia, E.; Wei, D.; Cui, P.; Ji, J.; Huang, H.; Jiang, H.; Dou, S.; Li, M.; Zhou, C.; Wang, W. Efficiency Enhancement with the Ferroelectric Coupling Effect Using P(VDF-TrFE) in $CH_3NH_3PbI_3$ Solar Cells. *Adv. Sci.* **2019**, *6*, No. 1900252.
(47) Cao, F.; Tian, W.; Meng, L.; Wang, M.; Li, L. Ultrahigh-Performance Flexible and Self-Powered Photodetectors with Ferroelectric P(VDF-TrFE)/Perovskite Bulk Heterojunction. *Adv. Funct. Mater.* **2019**, *29*, No. 1808415.
(48) Lee, M.; Jeong, B. Organic Ferroelectrics for Regulation of Electronic and Ionic Transport Toward Neuromorphic Applications. *Adv. Phys. Res.* **2025**, *4*, No. 2400087.
(49) Yagi, T.; Tatemoto, M.; Sako, J.-I. Transition Behavior and Dielectric Properties in Trifluoroethylene and Vinylidene Fluoride Copolymers. *Polym. J.* **1980**, *12*, 209.
(50) Furukawa, T.; Nakajima, T.; Takahashi, Y. Factors governing ferroelectric switching characteristics of thin VDF/TrFE copolymer films. *IEEE Trans. Dielectr. Electr. Insul.* **2006**, *13*, 1120.
(51) Jeong, B.; Gkoupidenis, P.; Asadi, K. Solution-Processed Perovskite Field-Effect Transistor Artificial Synapses. *Adv. Mater.* **2021**, *33*, No. 2104034.
(52) Park, Y. J.; Kang, S. J.; Park, C.; Lotz, B.; Thierry, A.; Kim, K. J.; Huh, J. Molecular and Crystalline Microstructure of Ferroelectric Poly(vinylidene fluoride-co-trifluoroethylene) Ultrathin Films on Bare and Self-Assembled Monolayer-Modified Au Substrates. *Macromolecules* **2008**, *41*, 109.
(53) Kim, K. L.; Lee, W.; Hwang, S. K.; Joo, S. H.; Cho, S. M.; Song, G.; Cho, S. H.; Jeong, B.; Hwang, I.; Ahn, J.-H.; Yu, Y.-J.; Shin, T. J.; Kwak, S. K.; Kang, S. J.; Park, C. Epitaxial Growth of Thin Ferroelectric Polymer Films on Graphene Layer for Fully Transparent and Flexible Nonvolatile Memory. *Nano Lett.* **2016**, *16*, 334.
(54) Hansen, K. R.; McClure, C. E.; Powell, D.; Hsieh, H.; Flannery, L.; Garden, K.; Miller, E. J.; King, D. J.; Sainio, S.; Nordlund, D.; Colton, J. S.; Whittaker-Brooks, L. Low Exciton Binding Energies and Localized Exciton−Polaron States in 2D Tin Halide Perovskites. *Adv. Opt. Mater.* **2022**, *10*, No. 2102698.
(55) Yang, L.; Fu, B.; Li, X.; Chen, H.; Li, L. Poly(vinylidene fluoride)-passivated $CsPbBr_3$ perovskite quantum dots with near-unity photoluminescence quantum yield and superior stability. *J. Mater. Chem. C* **2021**, *9*, 1983.
(56) Soulestin, T.; Ladmiral, V.; Dos Santos, F. D.; Améduri, B. Vinylidene fluoride- and trifluoroethylene-containing fluorinated electroactive copolymers. How does chemistry impact properties? *Prog. Polym. Sci.* **2017**, *72*, 16.
(57) Resende, P. M.; Isasa, J.-D.; Hadziioannou, G.; Fleury, G. Deciphering TrFE Fingerprints in P(VDF-TrFE) by Raman Spectroscopy: Defect Quantification and Morphotropic Phase Boundary. *Macromolecules* **2023**, *56*, 9673.
(58) Han, H.; Jeong, B.; Park, T. H.; Cha, W.; Cho, S. M.; Kim, Y.; Kim, H. H.; Kim, D.; Ryu, D. Y.; Choi, W. K.; Park, C. Highly Photoluminescent and Environmentally Stable Perovskite Nanocrystals Templated in Thin Self-Assembled Block Copolymer Films. *Adv. Funct. Mater.* **2019**, *29*, No. 1808193.
(59) Jeong, B.; Han, H.; Choi, Y. J.; Cho, S. H.; Kim, E. H.; Lee, S. W.; Kim, J. S.; Park, C.; Kim, D.; Park, C. All-Inorganic $CsPbI_3$ Perovskite Phase-Stabilized by Poly(ethylene oxide) for Red-Light-Emitting Diodes. *Adv. Funct. Mater.* **2018**, *28*, No. 1706401.
(60) Shepelin, N. A.; Sherrell, P. C.; Skountzos, E. N.; Goudeli, E.; Zhang, J.; Lussini, V. C.; Imtiaz, B.; Usman, K. A. S.; Dicinoski, G. W.; Shapter, J. G.; Razal, J. M.; Ellis, A. V. Interfacial piezoelectric polarization locking in printable $Ti_3C_2T_x$ MXene-fluoropolymer composites. *Nat. Commun.* **2021**, *12*, 3171.
(61) Su, Y.; Li, W.; Cheng, X.; Zhou, Y.; Yang, S.; Zhang, X.; Chen, C.; Yang, T.; Pan, H.; Xie, G.; Chen, G.; Zhao, X.; Xiao, X.; Li, B.; Tai, H.; Jiang, Y.; Chen, L. Q.; Li, F.; Chen, J. High-performance piezoelectric composites via β phase programming. *Nat. Commun.* **2022**, *13*, 4867.
(62) Islam, M. N.; Rupom, R. H.; Adhikari, P. R.; Demchuk, Z.; Popov, I.; Sokolov, A. P.; Wu, H. F.; Advincula, R. C.; Dahotre, N.; Jiang, Y.; Choi, W. Boosting Piezoelectricity by 3D Printing PVDF-MoS2 Composite as a Conformal and High-Sensitivity Piezoelectric Sensor. *Adv. Funct. Mater.* **2023**, *33*, No. 2302946.
(63) Shepelin, N. A.; Sherrell, P. C.; Goudeli, E.; Skountzos, E. N.; Lussini, V. C.; Dicinoski, G. W.; Shapter, J. G.; Ellis, A. V. Printed recyclable and self-poled polymer piezoelectric generators through single-walled carbon nanotube templating. *Energy Environ. Sci.* **2020**, *13*, 868.
(64) Kim, D.; Yang, Z.; Cho, J.; Park, D.; Kim, D. H.; Lee, J.; Ryu, S.; Kim, S.; Kim, M. High-performance piezoelectric yarns for artificial intelligence-enabled wearable sensing and classification. *EcoMater.* **2023**, *5*, No. e12384.
(65) Rosales, B. A.; Schutt, K.; Berry, J. J.; Wheeler, L. M. Leveraging Low-Energy Structural Thermodynamics in Halide Perovskites. *ACS Energy Lett.* **2023**, *8*, 1705−1715.
(66) Choi, J.; Le, Q. V.; Hong, K.; Moon, C. W.; Han, J. S.; Kwon, K. C.; Cha, P.-R.; Kwon, Y.; Kim, S. Y.; Jang, H. W. Enhanced Endurance Organolead Halide Perovskite Resistive Switching Memories Operable under an Extremely Low Bending Radius. *ACS Appl. Mater. Interfaces* **2017**, *9*, 30764.
(67) Wu, X.; Yu, H.; Cao, J. Unraveling the origin of resistive switching behavior in organolead halide perovskite based memory devices. *AIP Adv.* **2020**, *10*, No. 085202.
(68) Kerner, R. A.; Cohen, A. V.; Xu, Z.; Kirmani, A. R.; Park, S. Y.; Harvey, S. P.; Murphy, J. P.; Cawthorn, R. C.; Giebink, N. C.; Luther, J. M.; Zhu, K.; Berry, J. J.; Kronik, L.; Rand, B. P. Electrochemical Doping of Halide Perovskites by Noble Metal Interstitial Cations. *Adv. Mater.* **2023**, *35*, No. 2302206.

https://doi.org/10.1021/acsnano.4c07869
ACS Nano 2025, 19, 10796−10806

(69) Zhou, S.; Zhou, G.; Li, Y.; Xu, X.; Hsu, Y.-J.; Xu, J.; Zhao, N.; Lu, X. Understanding charge transport in all-inorganic halide perovskite nanocrystal thin-film field effect transistors. *ACS Energy Lett.* **2020**, *5*, 2614.
(70) Swift, M. W.; Lyons, J. L. First-Principles Survey of Acceptor Dopants for P-Type Cesium Lead Bromide. *J. Phys. Chem. C* **2022**, *126*, 12294−12300.
(71) Lyons, J. L.; Swift, M. W. Trends for Acceptor Dopants in Lead Halide Perovskites. *J. Phys. Chem. C* **2023**, *127*, 12735−12740.
(72) Kim, S. Y.; Yang, J. M.; Choi, E. S.; Park, N. G. Effect of interlayer spacing in layered perovskites on resistive switching memory. *Nanoscale* **2019**, *11*, 14330.
(73) Jeong, B.; Veith, L.; Smolders, T. J. A. M.; Wolf, M. J.; Asadi, K. Room-Temperature Halide Perovskite Field-Effect Transistors by Ion Transport Mitigation. *Adv. Mater.* **2021**, *33*, No. 2100486.
(74) Ghittorelli, M.; Lenz, T.; Sharifi Dehsari, H.; Zhao, D.; Asadi, K.; Blom, P. W. M.; Kovács-Vajna, Z. M.; de Leeuw, D. M.; Torricelli, F. Quantum tunnelling and charge accumulation in organic ferroelectric memory diodes. *Nat. Commun.* **2017**, *8*, 15741.
(75) Schroeder, U.; Park, M. H.; Mikolajick, T.; Hwang, C. S. The fundamentals and applications of ferroelectric HfO_2. *Nat. Rev. Mater.* **2022**, *7*, 653.
(76) Pradhan, D. K.; Moore, D. C.; Kim, G.; He, Y.; Musavigharavi, P.; Kim, K.-H.; Sharma, N.; Han, Z.; Du, X.; Puli, V. S.; Stach, E. A.; Joshua Kennedy, W.; Glavin, N. R.; Olsson, R. H.; Jariwala, D. *Nat. Electron.* **2024**, *7*, 348.
(77) Park, Y.; Kim, S. H.; Lee, D.; Lee, J. S. Designing Zero-Dimensional Dimer-Type All-Inorganic Perovskites for Ultra-Fast Switching Memory. *Nat. Commun.* **2021**, *12*, 3527.
(78) Kresse, G.; Furthmüller, J. Efficient Iterative Schemes for Ab Initio Total-Energy Calculations Using a Plane-Wave Basis Set. *Phys. Rev. B: Condens. Matter Mater. Phys.* **1996**, *54*, 11169−11186.
(79) Kresse, G.; Joubert, D. From Ultrasoft Pseudopotentials to the Projector Augmented-Wave Method. *Phys. Rev. B: Condens. Matter Mater. Phys.* **1999**, *59*, 1758−1775.
(80) Blöchl, P. E. Projector Augmented-Wave Method. *Phys. Rev. B: Condens. Matter Mater. Phys.* **1994**, *50*, 17953−17979.
(81) Perdew, J. P.; Burke, K.; Ernzerhof, M. Generalized Gradient Approximation Made Simple. *Phys. Rev. Lett.* **1996**, *77*, 3865−3868.
(82) Grimme, S.; Antony, J.; Ehrlich, S.; Krieg, H. A Consistent and Accurate Ab Initio Parametrization of Density Functional Dispersion Correction (Dft-D) for the 94 Elements H-Pu. *J. Chem. Phys.* **2010**, *132*, No. 154104.

https://doi.org/10.1021/acsnano.4c07869
ACS Nano 2025, 19, 10796−10806